The 8th International Supercritical CO_2 Power Cycles Symposium
February 27 – 29, 2024, San Antonio, Texas
Paper #50

Preliminary Sizing of Active Magnetic Bearings for sCO_2 Waste-Heat Recovery Application

Robert Lipham
Research Engineer
Southwest Research Institute
San Antonio, TX

Dongil Shin
Research Engineer
GE Vernova
Niskayuna, NY

Aaron Rimpel
Group Leader
Southwest Research Institute
San Antonio, TX

Amin Changizi
Sr. Research Engineer
GE Vernova
Niskayuna, NY

Dhanushkodi Durai Mariappan
Technology Manager
GE Vernova
Niskayuna, NY

Robert Lipham is a Research Engineer in the Machinery Department at Southwest Research Institute in San Antonio, Texas. He has been at Southwest Research Institute for over a year, and his work is primarily focused on the design and development of rotating machinery as well as electromechanical design. Some aspects of this work include mechanical design, electromagnetic modeling, and rotordynamic analysis. He earned both his Bachelor of Science and Master of Science degrees in Mechanical Engineering from Texas A&M University.

Dongil Shin holds a Bachelor of Science degree in Mechanical Engineering from Korea University in Seoul, South Korea. He also possesses a Master's degree in Aerospace and Mechanical Engineering from the University of California, Davis. He earned his Ph.D. in Mechanical Engineering from Texas A&M University in College Station, USA, in 2020. Currently, he serves as a research engineer at GE Vernova Advanced Research, where his technical research expertise spans damper design, mechanical design of rotating systems, rotordynamics analysis, and bearing modeling.

Aaron Rimpel is a Group Leader in the Machinery Department at Southwest Research Institute in San Antonio, Texas, where he has been for over 14 years. Mr. Rimpel and his Group within the Rotating Machinery Dynamics Section analyze problems associated with various types of machinery, design and develop rotating machinery components and systems, and develop component test stands for turbomachinery applications. Several aspects of this include rotordynamic analyses, structural/mechanical design, and software and diagnostic tool development for data collection and analysis. Mr. Rimpel obtained his Bachelor of Science degree in Mechanical Engineering from Western Michigan University and his Master of Science degree in Mechanical Engineering from Texas A&M University.

Amin Changizi received his Ph.D. degree from Concordia University, Montréal, QC, Canada, in 2011. He is currently a Senior Research Mechanical Engineer with General Electric Research Center, NY, USA. He is working on turbomachine designs. He was with different industries like Plug Power, MITI, Carrier Corporation. Prior to that, he was a part-time faculty member with Concordia University, Montréal. He has been a full-time faculty member for several years, and an engineer in various positions within the pump industry. His research interests are turbomachines, rotordynamics, theoretical nonlinear mechanics, Lie symmetry method with applications on nonlinear differential equations, and nonlinear behaviors of MEMS devices.

Dr. Dhanushkodi Durai Mariappan is the Technology Manager, Mechanical Systems and Design Lab at GE Research, Vernova R&D Center. His areas of expertise and research interests include printed electronics, nanomanufacturing, machine design, manufacturing, and dynamics. His recent work focus has been on three technologies/programs: superconducting generator, hydrogen storage, and printed sensors for crack detection. Dr. Mariappan received his undergraduate degree from the Indian Institute of Technology (IIT), Madras and Masters and Ph.D. degrees in Mechanical Engineering from the Massachusetts Institute of Technology (MIT). He is a member of the American Society of Mechanical Engineers (ASME) and American Society of Precision Engineering (ASPE) and has authored/co-authored over 40 technical papers and disclosures/patents.

ABSTRACT

The team of Southwest Research Institute (SwRI) and GE Vernova (GE) is executing a project developing conceptual designs of high-temperature active magnetic bearings (AMBs) for sCO_2 machinery applications. The goals of the project are to develop conceptual designs for radial and thrust AMBs capable of operating in sCO_2 environments up to 1000°F. A waste-heat recovery (WHR) application with hermetic machinery is used as a reference case to apply AMBs. This application was previously investigated to compare hermetic machinery enabled by process-lubricated bearings and high-speed motors/generators with traditional machinery configurations using oil-lubricated bearings, gearboxes, and grid-frequency electric machines.

In this paper, AMBs are sized for the WHR application machinery. Load capacity estimates are made using first-principle-derived formulas that consider operation at elevated temperatures. Estimates of linearized AMB system coefficients are also made to aid future controller development. Rotor models are developed that account for AMB rotor geometry and housing space requirements. Rotordynamics studies are performed to identify reasonable target values for closed-loop AMB stiffness and closed-loop AMB damping. These target values will be used in future control studies.

INTRODUCTION

A previous study [1] showed that hermetic machinery utilizing gas bearings for a notional 10 MWe sCO_2 power cycle drivetrain can provide order-of-magnitude reduction in power loss compared to conventional machinery utilizing oil-lubricated bearings, which has the potential for increasing overall cycle efficiency by several points. Like gas bearings, AMBs can operate in the process fluid and are, therefore, an alternative to enable hermetic machinery. AMBs are anticipated to have similar power loss and load capacity to gas bearings as well as offering the following advantages: greater tolerance to misalignments caused by tolerance stack-ups, thermal distortion, etc., due to order-of-magnitude larger clearances; the ability to tune stiffness and damping properties for stability and control of vibration amplitudes; “smart machine” and diagnostic ability; and high reliability due to lack of mechanical wear [2].

Gas bearing technology for MW-scale sCO_2 applications is technology readiness level (TRL) 3 or 4 since development has been on a functional sub-component level or in component rig tests in different environments than the final application. Current research is addressing the traditional limitations of gas bearings, namely low damping from the gas film and insufficient load capacity for larger turbomachines (e.g., journal diameters greater than 100 mm), by incorporating sealed oil squeeze film dampers and hydrostatic lift features [1, 3–5]. In contrast, AMB technology has significant commercial experience at that scale, though environments for high-performance sCO2 power cycle machinery conditions would be novel.

AMBs operating in sCO_2 up to 1020°F, a potential cooling temperature from the exhaust stream of a sCO_2 turbine, are not commercially available. However, feasibility at that temperature has been demonstrated in ambient-pressure air [6–8], making the AMB system TRL-4 for the present application. Others are developing 1020°F-capable AMBs for sCO_2 turbines [9], though some of this work is still in the preliminary phase [10]. A technical challenge with high-temperature AMBs for sCO_2 is material compatibility. Magnetic materials have property degradation and durability issues when operating at high temperature and/or in corrosive environments caused by corrosion, oxidation, thermal aging, creep, etc. [11]. Soft magnetic materials, such as FeCo for rotor laminations, show lower saturation flux density and reduced mechanical strength that lowers high-speed rotor capability. Insulation and other materials also require special consideration for high-temperature conditions, though ceramics and glass fiber composites have been demonstrated [6–8].

Ertas et al. [12–16] describe a WHR application employing a cascaded closed Brayton sCO_2 cycle to convert gas turbine exhaust stream heat to electric power. A benefit of cascaded sCO_2 cycles is their ability to function across a wider temperature range, differentiating them from single stage recuperated cycles. In the application for a natural gas compressor station, this power can be applied to a motor-driven compressor for additional capacity at the station, or it can be directed to the electricity grid. While the sCO_2 turbine inlet temperature for this specific application is only 869°F (waste-heat source of 950°F), the machinery is relevant for other applications, such as concentrating solar power, where turbine inlet temperatures would be in excess of 1290°F [17–20]. Moreover, the presented design utilizes hermetic machines operating on process-lubricated bearings. Therefore, this application is a natural case study to investigate the design of AMBs, which are a suitable alternative for a hermetic machine design.

Figure 1 shows a schematic of the WHR cycle from [12], which depicts two hermetic sCO_2 machines: a 12 krpm turbine-generator and a 27 krpm turbine-compressor with a motor/generator. Hereon, these may be referred to as the low-speed and high-speed machines, respectively. The low-speed turbine has eight axial stages, and the turbine and generator shafts are each supported by two journal bearings and joined with a flexible coupling—all in one hermetic casing. The high-speed machine has a single overhung radial compressor stage and a 3-stage axial turbine, and it is rigidly coupled to the motor/generator such that it has three journal bearings. In total, the two machines have seven journal bearings and two thrust bearings. Even though the machines are hermetic, seals are still utilized internally to reduce the pressure in the bearing chambers, which lowers the windage power loss and heat generation. The optimal cavity pressure was identified by modeling windage and the recompression power trade that results in the lowest net parasitic power loss.

The present paper considers the same machinery application as [12] and proposes to replace all process-lubricated bearings with AMBs. The scope is limited to preliminary sizing to demonstrate feasibility, including the considerations for the rotor construction and the dimensional considerations for the overall machine layout with AMBs. All features of the aerodynamic design and the internal seals are maintained for simplicity. Finally, while the example application does not require it, consideration of temperatures up to 1000°F will be included in the design to extend the conceptual design to other potential machines with similar physical requirements but higher temperatures.

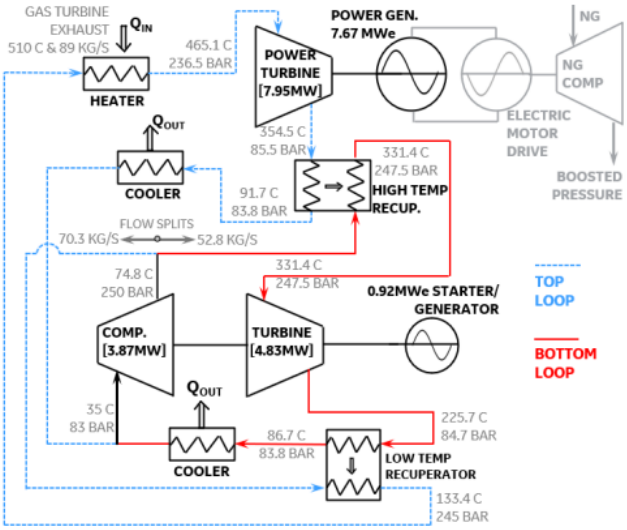

Figure 1. Cascaded closed Brayton sCO2 WHR cycle from [12]

METHODOLOGY

The design methodology for developing AMBs is an inherently iterative process. This is due to the fundamental interactions between load capacity requirements, AMB sizing, rotordynamics, and AMB control development. A general outline of the process used for this paper is shown in Figure 2.

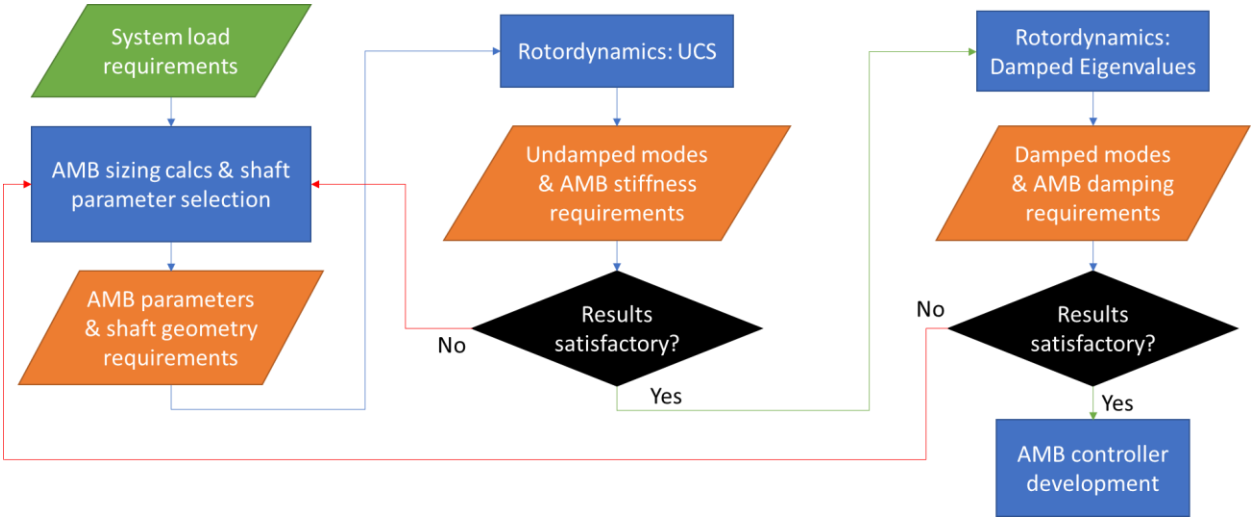

Figure 2: AMB design process flow chart

The starting point of this process is to define the load requirements for the machine. This will inform the initial AMB sizing efforts, which will, in turn, dictate the shaft geometry requirements. Once this step is completed, a rotordynamics model is developed, and an undamped critical speed (UCS) map is calculated for the system. This step allows inspection of the undamped system modes and initial selection of AMB closed-loop stiffnesses. If the results of this step are not satisfactory, either due to the existence of modes within the operating-speed range or unrealistically high closed-loop stiffness requirements, then further iterations of AMB sizing and shaft geometry adjustment can be undertaken. Otherwise, damped eigenvalues are computed

with the rotordynamics model using the closed-loop AMB stiffnesses selected in the UCS step. During this analysis, closed-loop AMB damping values are swept to determine the effect on overall rotor-bearing system stability and damped mode placement. If the results of this step are not satisfactory, either due to insufficient log decrement magnitudes with reasonable closed-loop AMB damping values or due to damped modes being pushed into the operating speed range, then further iterations of AMB sizing and shaft geometry adjustment can be undertaken. Otherwise, the next step in this process will involve more detailed controller development for the AMB-rotor system as a whole. The goal of the present study is to perform the steps needed to get to the control study stage and provide the necessary information (i.e., load capacity, AMB dynamic characteristics, etc.) required to perform that analysis in the future.

AMB LOAD REQUIREMENTS

Table 1 summarizes the initial AMB load capacity requirements for the low-speed and high-speed machines [12,16]. The total load requirement is estimated via Eq. (1).

$$F_{Total} = F_{Static} + F_{Dynamic} \tag{1}$$

For the radial bearings, imbalance studies can be used to refine the dynamic load requirements for each machine. However, for an initial estimate, the dynamic load capacity is set to be the same as the static load capacity [17]. For thrust bearings in a horizontal machine, the dynamic load capacity is set to zero. In both cases, the static load requirement is taken from [12] and [16].

Table 1: Bearing load capacity requirements

Machine	Bearing	Load Requirement	
		Static [lbf]	Total [lbf]
High-speed machine (27 krpm)	HS compressor	69	138
	HS thrust	2000	2000
	HS midspan	73	146
	HS generator	39	78
Low-speed machine (12 krpm)	LS turbine NDE	179	358
	LS turbine DE	289	578
	LS thrust	3500	3500
	LS generator DE	354	708
	LS generator NDE	320	640

AMB DESIGN APPROACH

To aid in sizing efforts, a force equation was derived for an 8-pole, heteropolar radial AMB. A general description of this type of bearing is shown in Figure 3. The full derivation is included in Appendix A, but the final result is Eq. (2). The assumptions made for this modeling effort were the standard magnetoquasistatic (MQS) assumptions [23], infinite core permeability compared to that of free space, and a small-enough air-gap to ignore fringing effects.

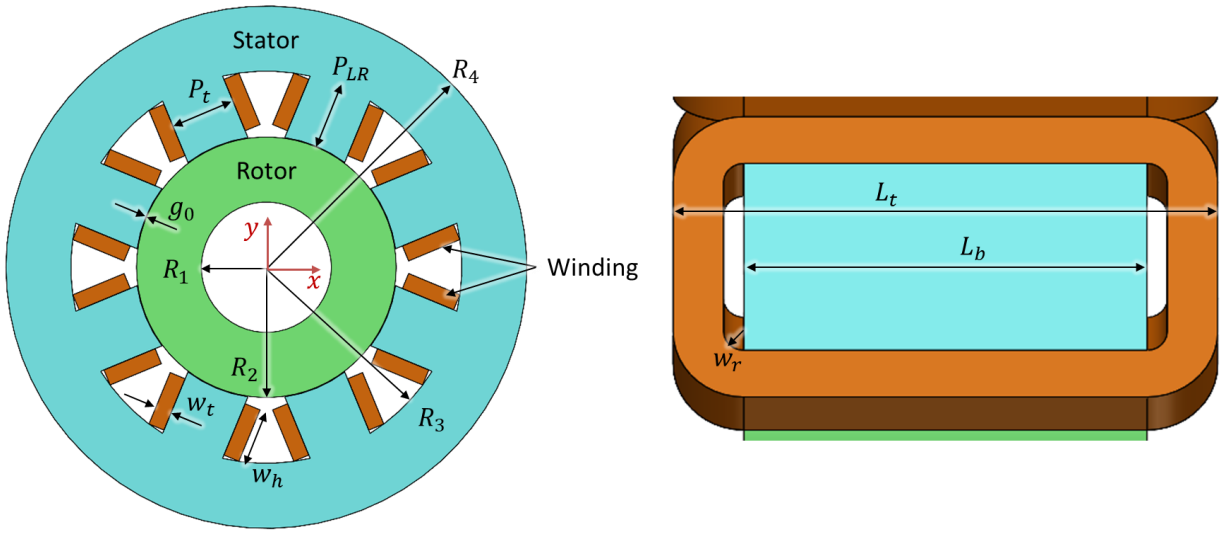

Figure 3: Diagram of a heteropolar, radial AMB

$$F_x = \frac{\mu_0 A_R N^2 \cos(\theta)}{4}\left(\frac{(I_b + I_c)^2}{(g_0 - x\cos(\theta))^2} - \frac{(I_b - I_c)^2}{(g_0 + x\cos(\theta))^2}\right) \tag{2}$$

where

$$A_R \triangleq P_t L_b \tag{3}$$

and, for an 8-pole AMB,

$$\theta \triangleq \frac{2\pi}{n_p} = \frac{\pi}{4}. \tag{4}$$

Note that N is the turn count per C-core winding and g_0 is the nominal radial gap when $x = 0$. The bias current, I_b, and the range of the control current, I_c, can both be defined in terms of the maximum current [22]. These relationships are described by Eqs. (5)–(7).

$$I_{max} \triangleq \frac{2 g_0 B_{sat}}{\mu_0 N} \tag{5}$$

$$I_b \triangleq \frac{1}{2} I_{max} = \frac{g_0 B_{sat}}{\mu_0 N} \tag{6}$$

$$-\frac{1}{2} I_{max} \leq I_c \leq \frac{1}{2} I_{max} \tag{7}$$

Here B_{sat} is the saturation flux density of the core material. Eqs. (6) and (7) can be used with Eq. (2) to estimate load capacity. For radial AMBs, the rated load capacity can be defined by the maximum force produced on a centered shaft, $x = 0$, with maximum control current, $I_c = \frac{1}{2} I_{max}$. When applied to Eq. (2), these conditions result in Eq. (8).

$$F_{x,c} = \frac{\mu_0 A_R N^2 I_{max}^2 \cos(\theta)}{4 g_0^2} \tag{8}$$

Equally important to the design of a radial AMB is the maximum liftoff force. Most machines that use AMBs are equipped with auxiliary bearings that are designed to hold the shaft when the AMBs are unpowered. When the shaft is resting on these auxiliary bearings, it is typically offset from the center position of the shaft by the radial clearance of the auxiliary bearings, x_c. An exaggerated example of this is shown in Figure 4.

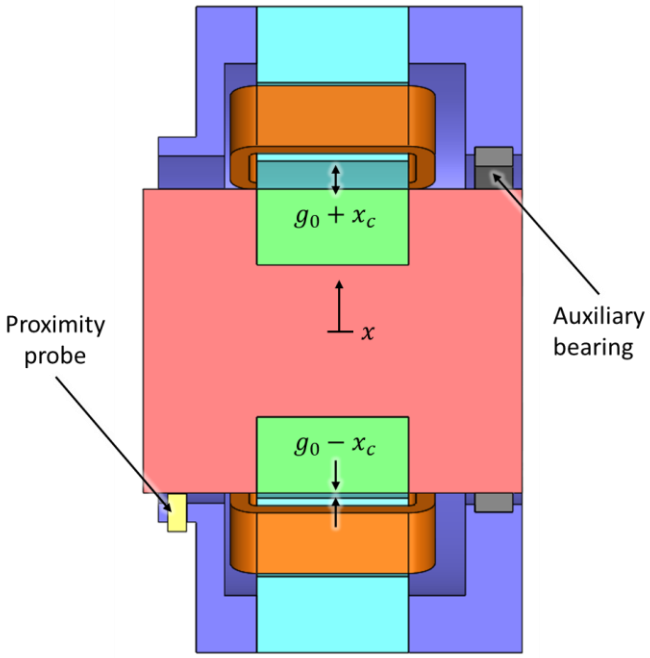

Figure 4: Exaggerated example of the liftoff condition for a radial AMB

In a horizontal machine, the liftoff force of the radial AMBs, defined as the force when $x = -x_c$ and $I_c = \frac{1}{2} I_{max}$, must be able to overcome the deadweight of the shaft. When applied to Eq. (2), these conditions result in Eq. (9).

$$F_{x,L} = \frac{\mu_0 A_R N^2 I_{max}^2 \cos(\theta)}{4(g_0 + x_c \cos(\theta))^2} \tag{9}$$

When comparing Eqs. (8) and (9), it is notable that, for the same input parameters, the maximum liftoff force will always be less than the maximum force at shaft center.

For the purposes of AMB control studies, it is useful to have a linearized force model. This can be achieved by applying a multivariable Taylor-series approximation to Eq. (2), where the linearizing points are defined at $x = 0$ and $I_c = 0$. The resulting equation takes the form of Eq. (10). Note that the open-loop position stiffness, K_x, is negative (i.e., The force generated is in the same direction as displacement), and it should not be conflated with the effective closed-loop stiffness of an AMB with a suitable control system.

$$F_x \cong K_x x + K_I I_c \tag{10}$$

where

$$K_x \triangleq \frac{\mu_0 A_R N^2 I_b^2 \cos^2(\theta)}{g_0^3} \tag{11}$$

and

$$K_I \triangleq \frac{\mu_0 A_R N^2 \cos(\theta) I_b}{g_0^2}. \tag{12}$$

Just as was done for the radial AMB, a force was also derived for a standard C-core thrust AMB. A general description of this type of bearing is shown in Figure 5.

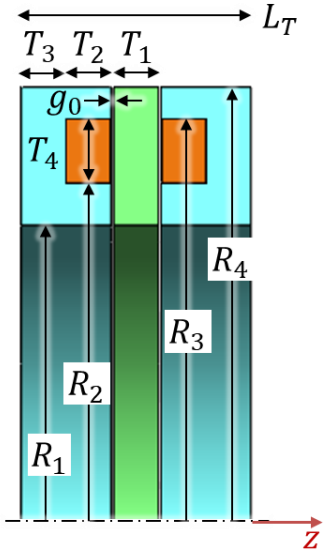

Figure 5: Diagram of a thrust AMB

If the same assumptions made for the radial AMB force model are used, then Eq. (13) can be used to estimate the force output of this type of AMB.

$$F_z = \frac{\mu_0 A_T N^2}{4}\left(\frac{(I_b + I_c)^2}{(g_0 - z)^2} - \frac{(I_b - I_c)^2}{(g_0 + z)^2}\right) \tag{13}$$

where, assuming the areas of both poles are constrained to be equal,

$$A_T = \pi(R_2^2 - R_1^2). \tag{14}$$

Note that N is the turn count per winding and g_0 is the nominal axial gap on one side of the rotor when $z = 0$. The bias current, I_b, and the range of the control current, I_c, can again both be described by Eqs. (6) and (7). For thrust AMBs, the rated load capacity can be defined by the maximum force produced on a centered shaft, $z = 0$, with maximum control current, $I_c = \frac{1}{2} I_{max}$. When applied to Eq. (13), these conditions result in Eq. (15).

$$F_{z,c} = \frac{\mu_0 A_T N^2 I_{max}^2}{4 g_0^2} \tag{15}$$

For a horizontal machine, the liftoff force for the thrust bearing is not as critical. However, it can still be derived using the same basic process as was used for the radial AMB. Applying a multivariable Taylor-series approximation to Eq. (13) with linearizing points $z = 0$ and $I_c = 0$ results in Eq. (16).

$$F_z \cong K_z z + K_I I_c \tag{16}$$

where

$$K_z \triangleq \frac{\mu_0 A_T N^2 I_b^2}{g_0^3} \tag{17}$$

and

$$K_I \triangleq \frac{\mu_0 A_T N^2 I_b}{g_0^2}. \tag{18}$$

Assuming the speed voltage is negligible, the voltage across the bearing windings can be described by the general form given in Eq. (19). While not immediately important to the rotordynamics, the inductance affects the bandwidth of the AMB-servo amplifier system, and the resistance affects the overall efficiency of the bearing.

$$V = L\frac{dI_c}{dt} + R(I_b + I_c) \tag{19}$$

where

$$L \triangleq \frac{\mu_0 A N^2}{2g_0}. \tag{20}$$

AMB DESIGN CONSTRAINTS AND MATERIAL SELECTION

The design requirements for the radial and thrust AMBs are summarized in Table 1. Looking at the equations provided thus far, there are several free parameters that can be adjusted to meet these load requirements. There are a couple of common constraints used to guide the selection of parameters. For radial bearings, it is common to attempt to minimize the axial length of the bearing to improve rotordynamics. Similarly, for thrust AMBs, it is best to minimize the diameter of the thrust disk to limit the rotating stresses applied to it. Both objectives are in direct opposition to maximizing load capacity of the AMBs since minimizing either radial AMB length or thrust AMB disk diameter lowers the pole area of the bearing. Similarly, it is desirable to limit the inductance and resistance of the AMB to both improve dynamic performance and reduce ohmic losses. However, both of these factors are dictated by the turn count of the windings, which positively affects load capacity. In short, the process of optimizing the AMB design for a particular application is not a trivial one, and there are a multitude of competing objectives that must be considered.

Table 2: Summary of bearing design requirements

AMB Type	Load requirement
Radial	$F_{x,c} > F_{Total}$
	$F_{x,L} > F_{Static}$
Thrust	$F_{z,c} > F_{Total}$

The total space required for an AMB is a concern that affects the layout of the machines being adapted. In addition to the physical space required for the AMB itself, space must also be included for auxiliary bearings and shaft proximity probes that provide position feedback for the AMB controller. As shown in Figure 4, this increases the axial length of a radial AMB. Similar effects also apply to the thrust AMBs. For either bearing type, additional space was included in the rotor models to account for these requirements.

Material selection is also of critical importance to AMB design as performance is dependent on high permeability and high saturation flux density. Hiperco® 50 has been selected as a material candidate for the magnetic bearings. The operating conditions of sCO_2 require good magnetic properties at 1000°F, and Hiperco® 50 is one of the few materials that can maintain high saturation flux density and high permeability at these elevated temperatures. However, the material properties of Hiperco® do change with temperature [24], so it is important to account for this when estimating force output. While the permeability does decrease, the values are still much larger than air, so the assumptions made for the previous analysis can still be considered valid. The saturation flux density decreases from 2.3 T at 73°F to 1.9 T at 1000°F. While this is a 17% decrease on its own, the maximum force output of the bearing is directly proportional to the square of the saturation flux density. This can be seen by substituting Eq. (5) into Eqs. (8) or (15). With all other factors being equal, the actual effect of this change in saturation flux density is an approximate 32% decrease in force output from center. To account for this temperature dependence, it was considered critical to use 1.9 T for the saturation flux density when calculating I_{max}.

AMB SIZING RESULTS

The first generation of AMB parameters were selected for both the low-speed and high-speed machines. The previously discussed design objectives and sizing constraints were applied during this process along with several geometric correlations to assure a relatively constant flux area throughout the AMBs. The geometric parameters are summarized in Tables 3 and 4.

Table 3: Summary of thrust AMB geometric parameters

Bearing	R_1 [in]	R_4 [in]	g_0 [in]	L_T [in]
HS thrust	2.00	3.56	0.020	2.65
LS thrust	2.50	4.17		2.80

Table 4: Summary of radial AMB geometric parameters

Bearing	R_1 [in]	R_2 [in]	R_4 [in]	g_0 [in]	L_b [in]	L_t [in]
HS compressor	1.10	1.50	2.82	0.015	2.00	2.51
HS midspan	1.65	2.15	3.57			
HS generator	1.10	1.50	2.82			
LS turbine NDE	1.70	2.30	3.82		2.50	3.01
LS turbine DE					3.30	3.81
LS generator DE					4.10	4.61
LS generator NDE						

The load ratings resulting from these parameters are summarized in Table 5. Note that the liftoff force calculations for the radial AMBs were computed from a rotor position of –0.005 in. The safety factors for static load capacity, primarily dictated by liftoff performance, all meet or exceed the given requirements for these machines. The same is true for the safety factors for total load capacity, which is primarily dictated by center force capability. However, several bearings have safety factors near unity, which will likely call for further sizing iterations. Nevertheless, this generation of AMB parameters was considered a good starting point for the rotordynamics studies.

Table 5: Summary of estimated AMB load ratings

Machine	Bearing	Static			Total		
		Req [lbf]	F_L [lbf]	SF	Req [lbf]	F_c [lbf]	SF
High-speed machine (27 krpm)	HS compressor	69	154	2.2	138	236	1.7
	HS thrust	N/A	N/A	N/A	2000	2,670	1.3
	HS midspan	73	193	2.6	146	295	2.0
	HS generator	39	154	4.0	78	236	3.0
Low-speed machine (12 krpm)	LS turbine NDE	179	289	1.6	358	442	1.2
	LS turbine DE	289	382	1.3	578	583	1.0
	LS thrust	N/A	N/A	N/A	3500	3,640	1.0
	LS generator DE	354	475	1.3	708	725	1.0
	LS generator NDE	320	475	1.5	640	725	1.1

The dynamic components for this generation of AMB parameters are summarized in Table 6. While not immediately useful to the set of rotordynamics studies that were undertaken in this paper, they will be important to future control studies. The inductances for the low-speed AMBs are worth discussing as they indicate future avenues for iteration. In particular, the low-speed generator AMBs have inductances of 84.8 mH. If the impedance is calculated at 200 Hz (12 krpm), the result is roughly 107 Ω. At 3.2 A of control current, this would lead to 342 V across

the windings of this AMB (not accounting for winding resistance). This control voltage requirement would likely cause issues in the selection of servo-amplifiers both in terms of absolute voltage level capability and bandwidth. A tradeoff that could be made would be to increase the control and bias current while decreasing the turn count of the windings. This would help to reduce the inductance and resistance, though the increased bias current would contribute more to ohmic losses. Again, this demonstrates a consideration for future design iterations.

Table 6: Summary of estimated AMB dynamic components

Machine	Bearing	K_p [lbf/in]	K_I [lbf/A]	I_b [A]	L [mH]
High-speed machine (27 krpm)	HS compressor	11,100	49.1	4.8	12.3
	HS thrust	134,000	506	5.3	108
	HS midspan	13,900	61.4	4.8	15.3
	HS generator	11,100	49.1	4.8	12.3
Low-speed machine (12 krpm)	LS turbine NDE	20,800	138	3.2	51.7
	LS turbine DE	27,500	182	3.2	68.3
	LS thrust	182,000	689	5.3	147
	LS generator DE	34,200	226	3.2	84.8
	LS generator NDE	34,200	226	3.2	84.8

ROTORDYNAMICS MODEL DEVLEOPMENT

As a preliminary step of the analysis, rotor models based on the original designs presented in [12] and [16] were developed. These models were tuned to match the UCS results from [12] and [16] to ensure that the material properties and rotor geometry, particularly those of the aero and generator sections, were matched as closely to the original models as possible. This was seen as an important step to ensure the relevance of the later rotor models that would be modified for AMB integration. Note that the laminations on the low-speed generator rotor were modeled with the density of silicon steel, but with zero stiffness. This was done to conservatively model the effective bending stiffness of the lamination section of the rotor.

The results of this tuning process are summarized and compared with the target results from [12] and [16] in Table 7. The results for all three rotor models showed good agreement with the target results with the exception of the 3rd mode for the high-speed machine. This mode, the 1st bending mode, was 11% lower than the target, and it is expected that this is due to possible differences in the connection constraints used in this model. Regardless, these results indicated that the developed rotor models were acceptable for the purpose of this study.

Table 7: Comparison of initial rotordynamics results with target results from [12]

	Mode	Freq. [cpm]	Target Freq. [cpm]	Percent Difference	Mode Type
High-speed machine (27 krpm)	1	6,962.3	7,041.9	–1.1%	Cylindrical
	2	8,956.9	9,047.9	–1.0%	Conical
	3	15,233.4	17,122.9	–11%	1st Bending
	4	35,821.1	3,5841.4	–0.1%	2nd Bending
Low-speed turbine (12 krpm)	1	5,690.8	5,661.9	0.5%	Cylindrical
	2	7,769.0	7,332.3	0.5%	Conical
	3	15,311.6	15,240.6	0.5%	1st Bending
Low-speed generator (12 krpm)	1	4,034	4,020	–0.3%	Cylindrical
	2	7,193	7,593	5.6%	Conical
	3	23,029	24,581	6.7%	1st Bending

ROTORDYNAMIC ANALYSIS WITH AMBS

The rotor designs from [12] and [16] were adapted to fit the AMBs developed from the first generation of parameters. All three rotors were modified for mounting rotor laminations and thrust bearing rotor disks. On the high-speed machine, the diameter was increased on the midspan side of the generator to maintain reasonable material thickness near the pilot fit. On the low-speed-turbine, the span was slightly reduced. Conversely, the span of the low-speed generator was slightly increased. The coupling interface diameter on both low-speed rotors was slightly decreased to allow for AMB rotor assembly. The modified machines are shown in Figures 6 and 7. Note that the thrust bearing locations remain the same as in the previous layouts in [12] and [16].

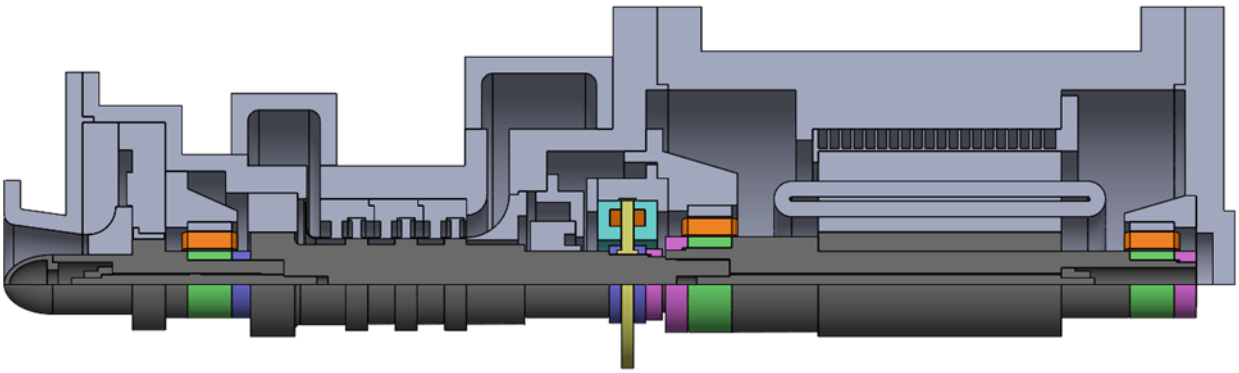

Figure 6: Updated high-speed machine (27 krpm) with AMBs

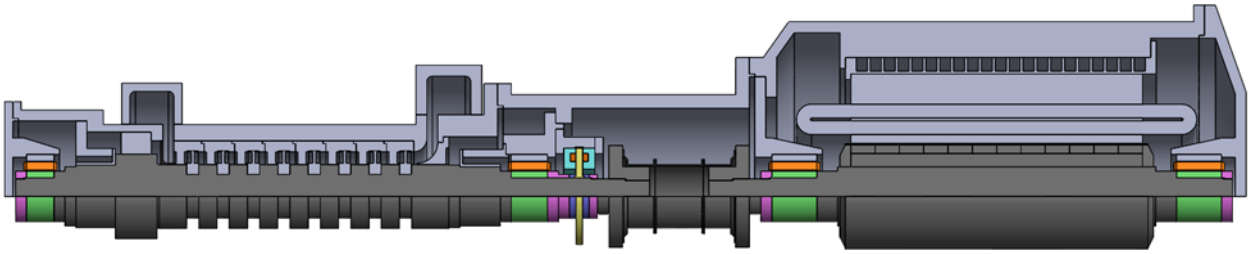

Figure 7: Updated low-speed turbine and generator (12 krpm) with AMBs

The design changes required for AMBs were also incorporated in the rotordynamics models for all three rotors. These changes can be seen in Figures 8–11. As was done for the low-speed generator laminations, the AMB rotor laminations, shown in green, were modeled with the density of Hiperco® 50, but with zero stiffness. This was again done to conservatively model the effective bending stiffness of the lamination section of the rotor.

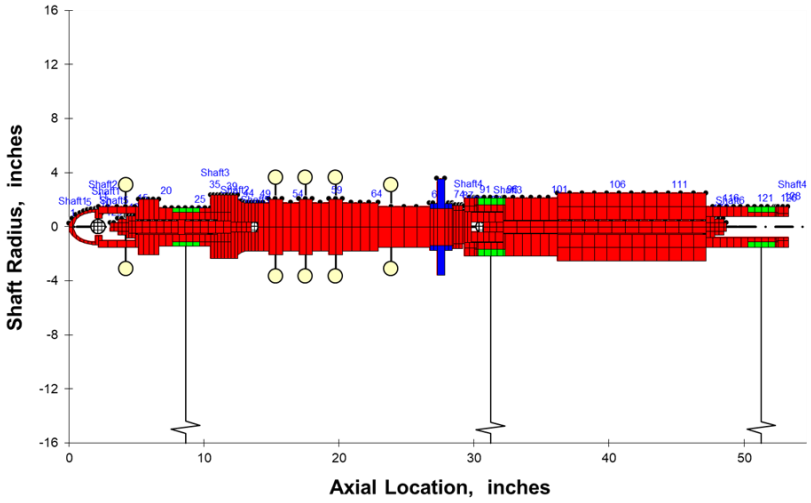

Figure 8: AMB high-speed machine (27 krpm) rotor model

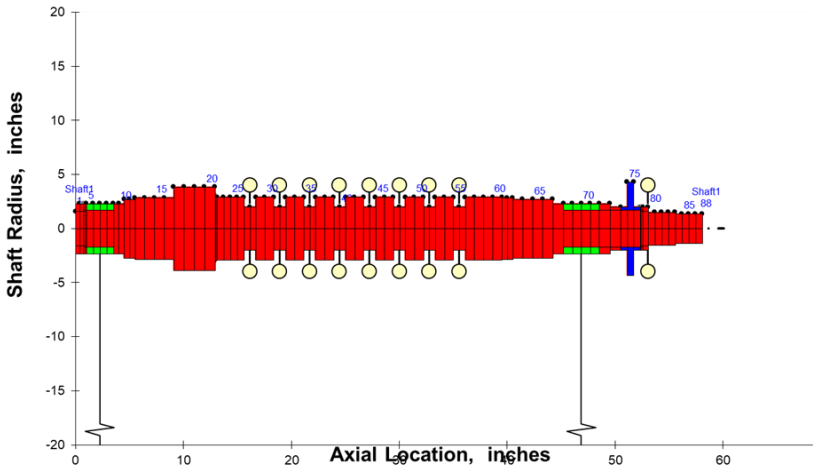

Figure 9: AMB low-speed turbine (12 krpm) model

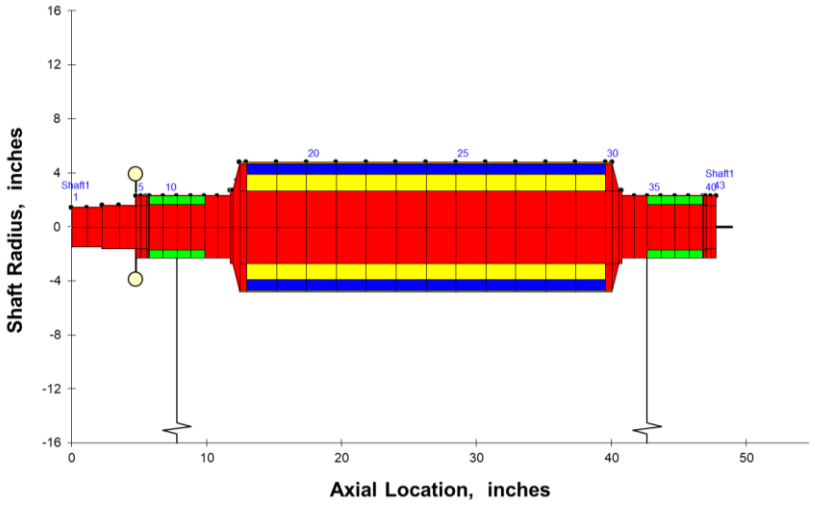

Figure 10: AMB low-speed generator (12 krpm) model

The UCS results for the AMB-modified rotors are summarized in Figures 11–13. Based on these results, the AMB closed-loop stiffness targets were set at 200,000 lbf/in for the high-speed machine and low-speed turbine, and 150,000 lbf/in for the low-speed generator. The resulting separation margins from the running speed to the next highest mode were 27.9% for the high-speed machine, 30.9% for the low-speed turbine, and 87.5% for the low-speed generator. These values were chosen by balancing the required AMB closed-loop stiffness with the separation margins.

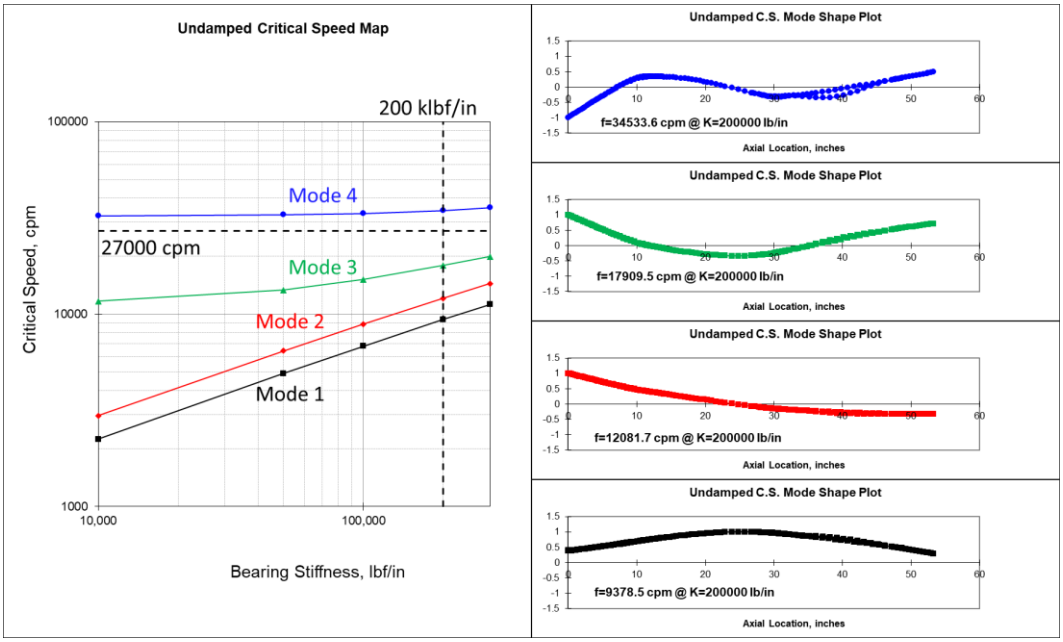

Figure 11: AMB high-speed machine (27 krpm) UCS and mode shapes

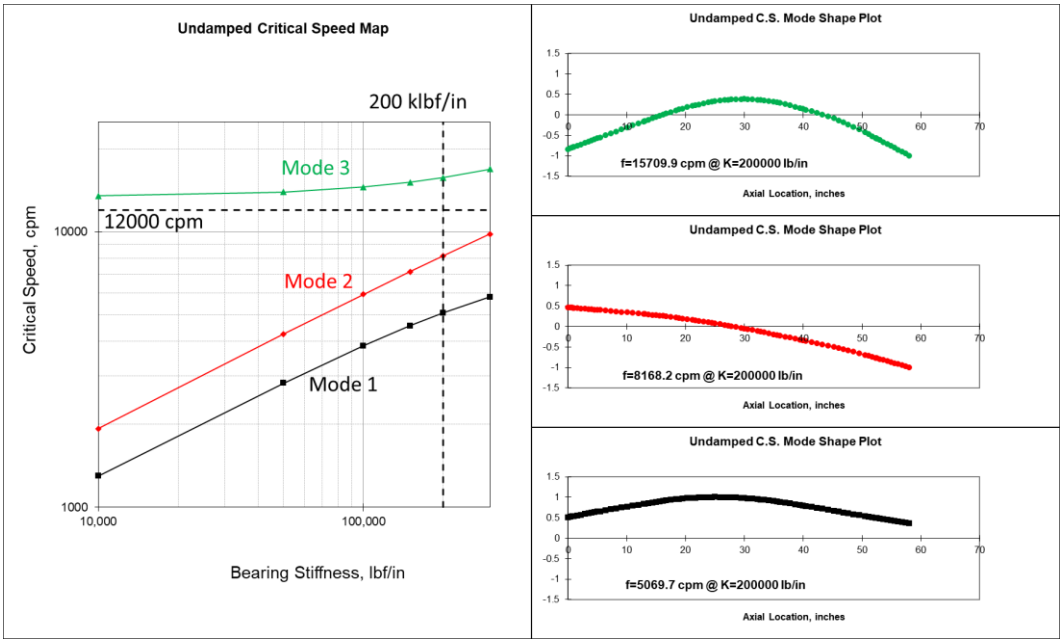

Figure 12: AMB low-speed turbine (12 krpm) UCS and mode shapes

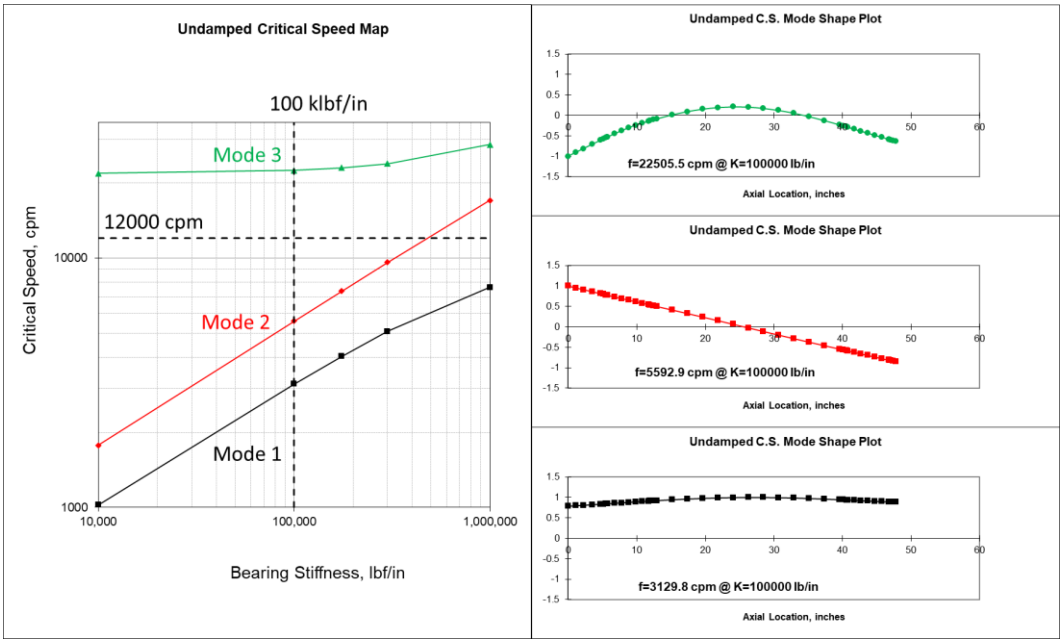

Figure 13: AMB low-speed generator (12 krpm) UCS and mode shapes

Both the selected closed-loop stiffnesses and undamped separation margins were considered reasonable for this application, so a damped eigenvalue analysis was pursued. Damping requirements were established from these results based on requirements for log decrement and damped mode separation margins. For the minimum requirements, API 617 requires a log decrement of 0.1 or greater for modes that exist below or up to the running speed [21]. For modes above the running speed, a log decrement of 0.0 or greater is required for modes with a 25% or greater separation margin [21]. While these requirements are an accepted industry

standard, the amount of uncertainty at this conceptual stage of design led to a more conservative log decrement target of 1.0 or greater for modes that exist below or up to the running speed.

The results of the damped eigenvalue analysis are summarized in Figures 14–16. The closed-loop AMB damping targets were selected from these results based on the previously discussed log decrement requirement. For the high-speed machine, a target value of 70 lbf-s/in was selected for the closed-loop AMB damping, and the resulting damped separation margin was 25.0%. For the low-speed turbine, a target value of 180 lbf-s/in was selected for the closed-loop AMB damping, and the resulting damped separation margin was 25.2%. For the low-speed generator, a target value of 125 lbf-s/in was selected for the closed-loop AMB damping, and the resulting damped separation margin was 86.0%. Note that, for closed-loop damping values selected between plotted points, a simple linear interpolation was used.

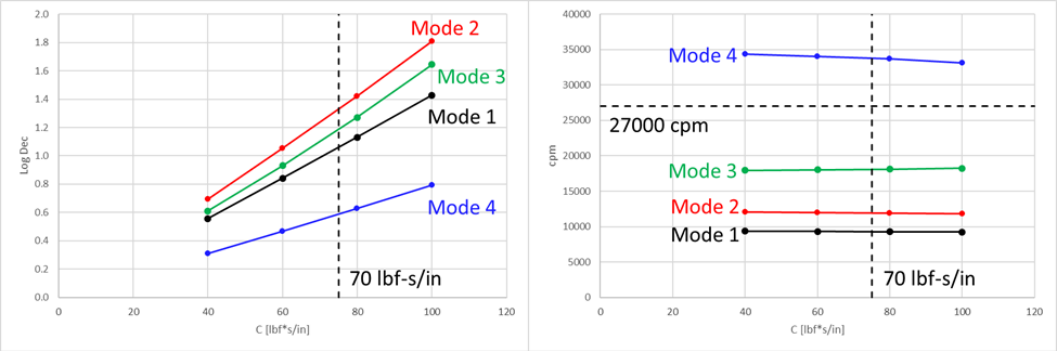

Figure 14: AMB high-speed machine (27 krpm) log decrement and damped natural frequency

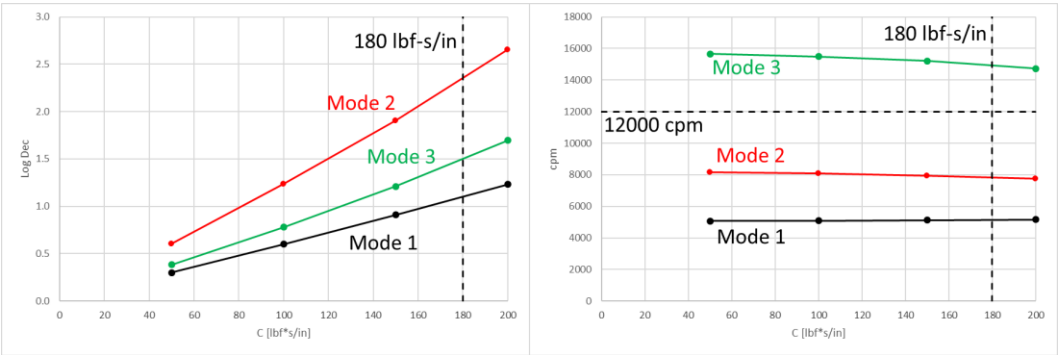

Figure 15: AMB low-speed turbine (12 krpm) log decrement and damped natural frequency

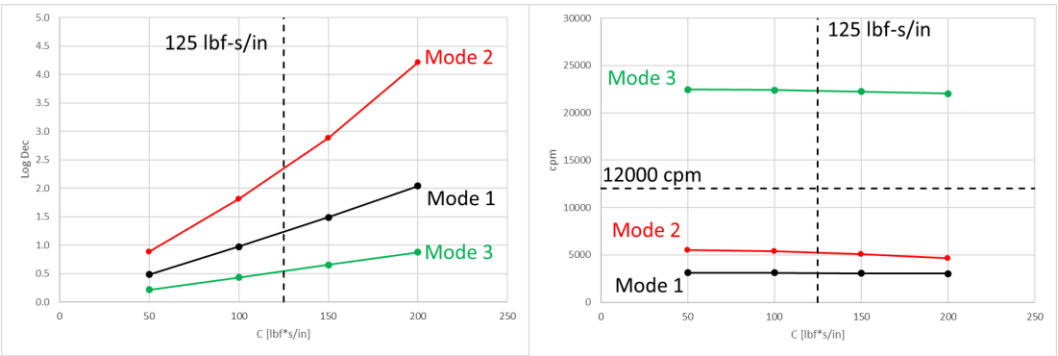

Figure 16: AMB low-speed generator (12 krpm) log decrement and damped natural frequency

Table 8 summarizes the resulting targets for both closed-loop AMB stiffness and closed-loop AMB damping from this generation of AMB parameters. From here, analysis could continue with further AMB conceptual design iteration or by proceeding to controller design. For AMB conceptual design, more focus could be put on minimizing actuator inductance, and further calculations could be included to estimate both ohmic losses in the windings and shaft windage losses. Otherwise, full-system controller models would need to be developed with the primary focus on achieving the desired targets for closed-loop stiffness and closed-loop damping.

Table 8: Summary of AMB closed-loop rotordynamic coefficient targets

Rotor	Radial Bearing	Required Closed-Loop Stiffness [lbf/in]	Required Closed-Loop Damping [lbf-s/in]	Damped Separation Margin
High-speed machine (27 krpm)	HS compressor	200,000	70.0	25.0%
	HS midspan			
	HS generator			
Low-speed turbine (12 krpm)	LS turbine NDE	200,000	180	25.2%
	LS turbine DE			
Low-speed generator (12 krpm)	LS generator DE	100,000	125	86.0%
	LS generator NDE			

CONCLUSIONS

Preliminary AMB sizing calculations were performed using the machinery for a WHR application as a case study. The machinery includes a low-speed (12 krpm) turbine-generator and a high-speed (27 krpm) turbine-compressor with a motor/generator. Both machines are also hermetic, which has performance advantages with regards to sealing requirements, enabled by process-lubricated bearings that are replaced with AMBs in this study. The low-speed machine train includes four radial bearings and one axial bearing, and the high-speed machine includes three radial bearings and one thrust bearing. The rotor designs for the WHR machines were modified to include the features of the AMBs, and rotordynamic studies were performed to identify the closed-loop stiffness and closed-loop damping targets for the AMBs. While the example WHR application does not require it, the AMB analysis considered design temperatures up to 1000°F to extend the conceptual design to other potential machines with similar physical requirements but higher temperatures. This was accomplished by using the saturation flux density of the bearing core material at 1000°F to constrain the maximum allowable AMB current. The result of this was a limitation of AMB force output based on the material properties of the core material.

The work in this paper represents the preliminary conceptual design effort. Further work is required to advance the design. For example, magnetic FEA should be employed to increase prediction fidelity and accuracy, and in-depth control modeling will be required to ensure that the targeted closed-loop stiffness and closed-loop damping values are achievable. This would also need to include transient and off-design performance evaluation in addition to steady state performance. In conjunction, rotordynamics analyses will also need to be refined with updated AMB models and other dynamic effects from seals, impellers, etc., to confirm overall

performance. Finally, development of the catcher bearings should include dropped rotor simulations.

ACKNOWLEDGEMENT AND DISCLAIMER

This material is based upon work supported by the U.S. Department of Energy's Office of Energy Efficiency and Renewable Energy (EERE) under the Solar Energy Technologies Office, Award Number DE-EE0009823.

REFERENCES

[1] Ertas, B., 2019, "Compliant Hybrid Gas Bearing Using Integral Hermetically Sealed Squeeze Film Dampers," J. Eng. Gas Turb. Power, 141(10), pp. 101020.

[2] Rimpel, A., Smith, N., Allison, T., and Masala, A., 2020, "Magnetic Bearings for High-Temperature sCO_2 Pumped Heat Energy Storage," GT2020-15747, Proc. ASME Turbo Expo 2020.

[3] Ertas, B., and Delgado, A., 2019, "Hermetically Sealed Squeeze Film Damper for Operation in Oil-Free Environments," J. Eng. Gas Turb. Power, 141(2), pp. 022503-1.

[4] Ertas, B., Gary, K., and Delgado, A., 2020, "Additively Manufactured Compliant Hybrid Gas Thrust Bearing for sCO_2 Turbomachinery: Experimental Evaluation and Fluid-Structure Model Predictions," GT2020-14964, Proc. ASME Turbo Expo 2020.

[5] Ertas, B., 2021, "Additively Manufactured Compliant Hybrid Gas Thrust Bearing for Supercritical Carbon Dioxide Turbomachinery: Design and Proof of Concept Testing," J. Eng. Gas Turb. Power, 143, pp. 081023.

[6] Provenza, A. J., Montague, G. T., Jansen, M. J., Palazzolo, A. B., and Jansen, R. H., 2005, "High Temperature Characterization of a Radial Magnetic Bearing for Turbomachinery," ASME J. Eng. Gas Turbines and Power, 127(4), pp. 437-444.

[7] Palazzolo, A., Tucker, R., Kenny, A., Kang, K., Ghandi, V., Liu, J., Choi, H., and Provenza, A., 2008, "High Temperature, Permanent Magnet Biased, Fault Tolerant, Homopolar Magnetic Bearing Development," Paper No. GT2008-50917, Proceedings of ASME Turbo Expo 2008, June 9-13, Berlin, Germany.

[8] Liu, J., Choi, H., Palazzolo, A., Tucker, R., Kenny A., Kang, K., Ghandi, V., and Provenza, A., 2008, "High Temperature Hybrid Radial Magnetic Bearing Systems Capable of Operating up to 538°C (1,000°F)," 20th International Workshop on Rare Earth Magnets and Their Applications (REPM08), Greece, EEC Conference Paper REPM08, September 8-10.

[9] Choi, H., and Palazzolo, A., "Ultra High-Temperature Magnetic Bearing System for s-CO_2 Turbines/Expanders," DE-SC0018813.

[10] Lipham, R., Choi, H., Bielefeld, M., Shin, Dongil., Thomas, Erwin., Palazzolo, A., Tucker, R., F., "Design of a Permanent Magnet Biased Homopolar Magnetic Bearing for SCO2 Turbine

Applications," Supercritical CO2 Power Cycles Symposium, San Antonio, TX, Feb. 26-29, 2024. (Publication under review.)
[11] Vannini, A., Marfoli, A., Papini, L., Bolognesi, P., and Gerada, C., 2021, “Materials for Electric Machines Suited for High-Temperature Applications: A Survey,” IEEE Workshop on Electrical Machines Design, Control and Diagnosis, 8-9 April, Modena, Italy.
[12] Ertas, B, Zierer, J, McClung, A, Torrey, D, Bidkar, RA, Hofer, D, Rallabandi, V, Singh, R, & Zhang, X. "Super-Critical Carbon Dioxide Power Cycle for Waste Heat Recovery Utilizing Hermetic Oil-Free Turbomachinery: Cycle and Conceptual Turbomachinery Design." Proceedings of the ASME Turbo Expo 2023: Turbomachinery Technical Conference and Exposition. Volume 12: Supercritical CO_2. Boston, Massachusetts, USA. June 26–30, 2023. V012T28A033. ASME.
[13] Ertas, B., Powers, J., Gary, K., Torrey, D., Zierer, J., Baehmann, P., Rallabandi, V., Adcock, T., Anandika, N., & Bidkar, R. A. (2023). Test Rig Concept for Evaluating the Performance of a CO_2 Immersed Electro-Mechanical Rotor System Utilizing Gas Bearings: Part-1 Mechanical and Electric Machine Design. ASME
[14] Ertas, B., Gary, K., & Adcock, T. a. A. (2023). Identification of Dynamic Force Coefficients for an Additively Manufactured Hermetic Squeeze Film Bearing Support Damper Utilizing a Pass-Through Channel. ASME.
[15] Bidkar, R. A., Kumar, U., Zhang, X., Sarawate, N., Powers, J., Anandika, N. M., & Ertas, B. (2023). Test Rig Concept for Evaluating the Performance of a CO_2 Immersed Electromechanical Rotor System Utilizing Gas Bearings: Part-2 Thermal Systems & Flow Loop Design. ASME.
[16] Ertas, B. (2019, November 6). *Novel Modular Heat Engines with* sCO_2 *Bottoming Cycle Utilizing Advanced Oil Free Turbomachinery DOE FE0031617: Phase 1* [Design overview presentation]. 2019 University Turbine Systems Research Project Review Meeting. Orlando, FL, United States.
[17] Kleynhans, G., Pfrehm, G., Berger, H., & Baudelocque, L. (2005). Hermetically Sealed Oil-Free Turbocompressor Technology. Turbomachinery and Pump Symposia, 2005.
[18] Cich, S. D., Moore, J., Mortzheim, J. P., Hofer, D., “Design of a Supercritical CO_2 Compressor for Use in a 10Mwe Power Cycle”, Proceedings of the 6th International Supercritical CO_2 Power Cycles Symposium, Pittsburgh, PA, March 27-29, 2018.
[19] Moore, J. J., Cich, S., Day-Towler, M., Hofer, D., Mortzheim, J., “Testing of a 10Mwe Supercritical CO_2 Turbine”, Proceedings of the 47th Turbomachinery and 34th Pump Symposia, Houston, TX, September 17-20, 2018.
[20] Cich, S. D., Moore, Kulhanek, C., J., Mortzheim, J. P., “Development and Testing of a Supercritical CO_2 Compressor Operating near the Dome”, Proceedings of the Turbomachinery and Pump Symposia, Sept. 15-17, 2020.
[21] API 617 Ninth Edition., April 2022, Axial and Centrifugal Compressors and Expander-Compressors
[22] Bleuler, Hannes, Matthew Cole, Patrick Keogh, Rene Larsonneur, Eric Maslen, Y. Okada, G. Schweitzer, and A. Traxler. Magnetic bearings: theory, design, and application to rotating machinery. Springer Science & Business Media, 2009.
[23] Melcher, J. R., & Woodson, H. (1968). Electromechanical Dynamics Part I: Discrete Systems.
[24] De Groh, H. C., Geng, S. M., Niedra, J. M., & Hofer, R. R. (2018). Magnetic Properties of Fe-49Co-2V Alloy and Pure Fe at Room and Elevated Temperatures. NASA.

NOMENCLATURE

Parameter	Definition
θ	Pole angle
λ	Magnetic flux linkage
μ_0	Permeability of free space
Φ	Magnetic flux
A	Pole area
A_R	Radial pole area
A_T	Axial pole area
B	Magnetic flux density
B_{sat}	Saturation flux density of a material
E_s	Speed-voltage factor
F	Force
$F_{Dynamic}$	Dynamic load requirement
F_{Static}	Static load requirement
F_{Total}	Total load requirement
F_x	X-axis force output
$F_{x,c}$	X-axis load capacity at shaft position $x = 0$
$F_{x,L}$	X-axis load capacity at shaft position $x = x_c$
F_z	Z-axis force output
$F_{z,c}$	Z-axis load capacity at shaft position $z = 0$
g	Air gap
g_0	Nominal air gap (single-sided)
H	Magnetic field intensity
I	Current
I_b	Bias current
I_c	Control current
I_{max}	Maximum total current
J	Current density
K_I	Current stiffness
K_x	X-axis negative position stiffness
K_z	Z-axis negative position stiffness
L	Winding inductance

Parameter	Definition
N	Per-winding turn count
n_p	Magnetic bearing pole count
R	Winding resistance
V	Winding voltage
w'	Co-energy
x	Shaft radial position (for single axis motion)
x_c	Shaft position offset when resting on auxiliary bearings
z	Shaft axial position

APPENDIX A: DERIVATION OF MAGNETIC BEARING FORCE EQUATIONS

The general model of a C-core actuator shown in Figure 17.

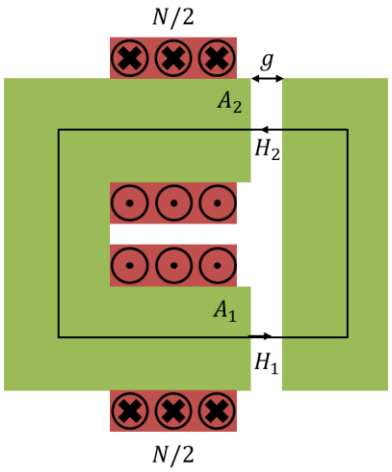

Figure 17: General model of a C-core actuator

If the MQS assumptions [23] are applied, then the integral form of Maxwell's equations can be defined as by Eqs. (21)–(23).

$$\oint_c \boldsymbol{H} \cdot d\boldsymbol{l} = \int_S \boldsymbol{J} \cdot d\boldsymbol{a} = NI \tag{21}$$

$$\oint_s \boldsymbol{B} \cdot d\boldsymbol{a} = 0 \tag{22}$$

$$\oint_S \boldsymbol{J} \cdot d\boldsymbol{a} = 0 \tag{23}$$

In addition to the MQS assumptions, several other assumptions can be made to simplify the analysis. First, it can be assumed that the magnetic field intensity, H, is zero inside the core so long as the core permeability is so much larger than the permeability of free space that it can be assumed to be practically infinite. Second, the air gap is assumed to be small enough that the effects of fringing fields are negligible. Third, the fields within the gap are assumed to be uniformly distributed. Applying these assumptions to Eqs. (21) results in (24).

$$H_1 g + H_2 g = NI \tag{24}$$

Applying Eq. (22) yields Eq. (25).

$$B_1 A_1 - B_2 A_2 = 0 \ \rightarrow H_2 = \frac{A_1}{A_2} H_1 \tag{25}$$

Substituting Eq. (25) into Eq. (24) yields Eq. (26).

$$H_1 = \frac{NI}{g\left(1 + \frac{A_1}{A_2}\right)} \tag{26}$$

From Eq. (26), the flux can be defined by Eq. (27).

$$\Phi = B_1 A_1 = \mu_0 H_1 A_1 = \frac{\mu_0 NI}{g\left(\frac{1}{A_1} + \frac{1}{A_2}\right)} \tag{27}$$

The flux linkage can be defined by Eq. (28) [23].

$$\lambda \triangleq \int_S NB \cdot da = N\Phi = \frac{\mu_0 N^2 I}{g\left(\frac{1}{A_1} + \frac{1}{A_2}\right)} \tag{28}$$

The co-energy can be defined by Eq. (29) [23].

$$w' = \int_0^I \lambda(I')dI' = \frac{\mu_0 N^2 I^2}{2g\left(\frac{1}{A_1} + \frac{1}{A_2}\right)} \tag{29}$$

The force can then be found via Eq. (30) [23].

$$F = \frac{\partial w'}{\partial g} = -\frac{\mu_0 N^2 I^2}{2g^2\left(\frac{1}{A_1} + \frac{1}{A_2}\right)} \tag{30}$$

where the negative sign indicates and attractive force between the core and bar. Assuming the area of both poles is equal, the force takes the general form of Eq. (31).

$$F = -\frac{\mu_0 A N^2 I^2}{2g^2} \tag{31}$$

Consequentially, the flux density can be described by Eq. (32).

$$B = \frac{\mu_0 N I}{2g} \tag{32}$$

If the saturation flux density of the core material, B_{sat}, is used as the limiting factor, then the maximum current can be set by Eq. (33) [22].

$$I_{max} = \frac{2gB_{sat}}{\mu_0 N} \tag{33}$$

Assuming the area of both poles is equal, the flux linkage can be re-written as Eq. (34).

$$\lambda = \frac{\mu_0 A N^2 I}{2g} \tag{34}$$

The coil voltage, assuming the windings are in series, can be found by taking the time derivative of the flux linkage [23].

$$V = \frac{d\lambda}{dt} = L\frac{dI}{dt} - E_s\frac{dg}{dt} \tag{35}$$

where

$$L \triangleq \frac{\mu_0 A N^2}{2g} \tag{36}$$

and

$$E_s \triangleq \frac{\mu_0 A N^2}{2g^2}. \tag{37}$$

The contributions from the back EMF are typically ignored for AMBs, but the inductance can play an important role in the servo amplifier dynamics. Note that winding resistance is ignored here as well.

Eqs. (31)–(33) and (36) can be used to model most C-core actuators that fit the assumptions made thus far. These formulae can be extended to opposing C-core actuators, which are of interest for AMB calculations. Figure 18 shows a general description of this arrangement. In this case, x denotes the position of the center bar, and g_0 denotes the nominal gap when $x = 0$. Both actuators are assumed to have the same number of turns, N, and pole area, A. It is worth noting that (36) is a useful approximation for opposing C-core actuators as well, though cross-coupling effects between windings may exist depending on the topology. In such cases, a more rigorous analysis would be necessary to quantify the inductance matrix of the entire system.

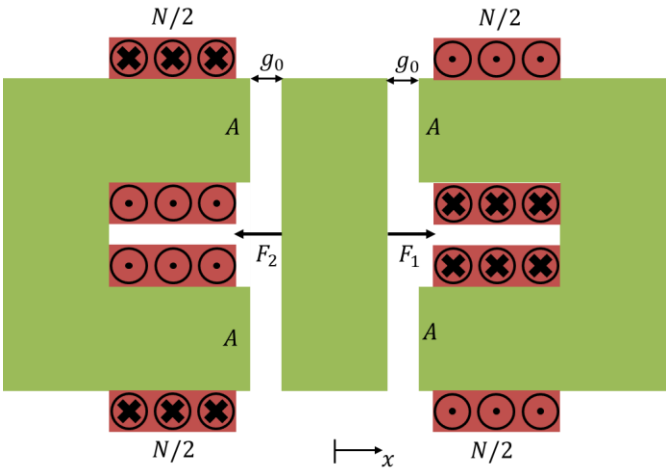

Figure 18: Opposing C-core actuator model

Applying Eq. (31), the forces can be described Eqs. (38) and (39).

$$F_1 = \frac{\mu_0 A N^2 I_1^2}{2g_1^2} \tag{38}$$

$$F_2 = \frac{\mu_0 A N^2 I_2^2}{2g_2^2} \tag{39}$$

Here:

$$I_1 \triangleq I_b + I_c \tag{40}$$

$$I_2 \triangleq I_b - I_c \tag{41}$$

$$g_1 = g_0 - x \tag{42}$$

$$g_2 = g_0 + x \tag{43}$$

The bias current, I_b, is static, and it's provided to help linearize the response. From Eqs. (38)–(43), the sum of forces on the center bar can by described by Eq. (44).

$$F = F_1 - F_2 = \frac{\mu_0 A N^2}{2}\left(\frac{(I_b + I_c)^2}{(g_0 - x)^2} - \frac{(I_b - I_c)^2}{(g_0 + x)^2}\right) \tag{44}$$

Eq. (44) can be used to find the force output of a thrust magnetic bearing merely by substituting the appropriate pole area. This result can be further extended by considering the case where an actuator's poles are not parallel. As shown in Figure 19, this occurs in a typical C-core radial magnetic bearing. The projection shown in Figure 19, when substituted into Eq. (44), results in Eq. (45).

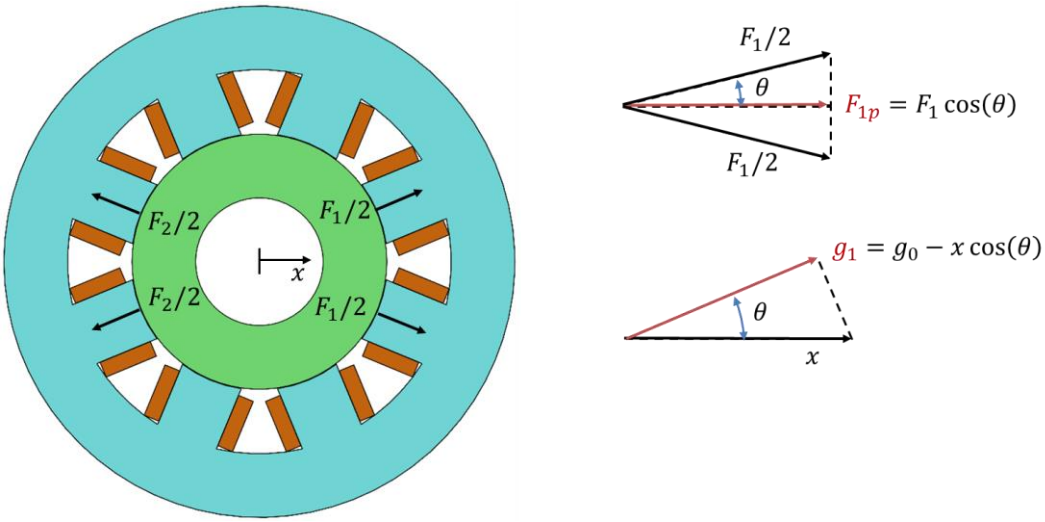

Figure 19: Example radial AMB force and gap projection.

$$F_x = \frac{\mu_0 A_R N^2 \cos(\theta)}{4}\left(\frac{(I_b + I_c)^2}{(g_0 - x\cos(\theta))^2} - \frac{(I_b - I_c)^2}{(g_0 + x\cos(\theta))^2}\right) \tag{45}$$

It is worth noting that these equations are a useful approximation for the initial sizing of AMBs, However, the inability of this modeling to capture fringing fields and the effects of a saturated core should not be ignored. Further, this model fails to include the effects of eddy current losses, which can be a significant factor in certain AMB topologies. Further modelling with FEA is generally recommended for more accurate performance prediction.